

# The origin of the soft excess in the luminous quasar HE 1029-1401

B. Vaia<sup>1,2,3</sup>, F. Ursini<sup>4</sup>, G. Matt<sup>4</sup>, D.R. Ballantyne<sup>5</sup>, S. Bianchi<sup>4</sup>, A. De Rosa<sup>6</sup>, R. Middei<sup>7,8</sup>, P.O. Petrucci<sup>9</sup>,  
E. Piconcelli<sup>7</sup> and A. Tortosa<sup>7</sup>

<sup>1</sup> Scuola Universitaria Superiore IUSS Pavia, Piazza della Vittoria 15, 27100 Pavia, Italy  
e-mail: [beatrice.vaia@iusspavaia.it](mailto:beatrice.vaia@iusspavaia.it)

<sup>2</sup> Department of Physics, University of Trento, Via Sommarive 14, 38123 Povo (TN), Italy

<sup>3</sup> Istituto Nazionale di Astrofisica, Istituto di Astrofisica Spaziale e Fisica Cosmica di Milano, via A. Corti 12, 20133 Milano, Italy

<sup>4</sup> Dipartimento di Matematica e Fisica, Università degli Studi Roma Tre, via della Vasca Navale 84, 00146, Roma, Italy

<sup>5</sup> Center for Relativistic Astrophysics, School of Physics, Georgia Institute of Technology, 837 State Street, Atlanta, GA 30332-0430, USA

<sup>6</sup> INAF Istituto di Astrofisica e Planetologia Spaziali, Via del Fosso del Cavaliere 100, I-00133 Roma, Italy

<sup>7</sup> INAF - Osservatorio Astronomico di Roma, Via Frascati 33, I-00040 Monte Porzio Catone, Italy

<sup>8</sup> Space Science Data Center, SSDC, ASI, Via del Politecnico snc, I-00133 Roma, Italy

<sup>9</sup> Univ. Grenoble Alpes, CNRS, IPAG, 38000 Grenoble, France

Received; accepted

## ABSTRACT

The enigmatic and intriguing phenomenon of the "soft excess" observed in the X-ray spectra of luminous quasars continues to be a subject of considerable interest and debate in the field of high-energy astrophysics. This study focuses on the quasar HE 1029-1401 ( $z = 0.086$ ,  $\log(L_{\text{bol}}/[\text{erg s}^{-1}]) = 46.0 \pm 0.2$ ), with a particular emphasis on investigating the properties of the hot corona and the physical origin of the soft excess. In this study, we present the results of a joint *XMM-Newton/NuSTAR* monitoring campaign of this quasar conducted in May 2022. The source exhibits a cold and narrow Fe  $K\alpha$  emission line at 6.4 keV, in addition to the detection of a broad component. Our findings suggest that the soft excess observed in HE 1029-1401 can be adequately explained by Comptonized emission originating from a warm corona. Specifically, fitting the spectra with two `NTHCOMP` component we found that the warm corona is characterized by a photon index ( $\Gamma^w$ ) of  $2.75 \pm 0.05$  and by an electron temperature ( $kT_e^w$ ) of  $0.39^{+0.06}_{-0.04}$  keV, while the optical depth ( $\tau^w$ ) is found to be  $23 \pm 3$ . We also test more physical models for the warm corona, corresponding to two scenarios: pure Comptonization and Comptonization plus reflection. Both models provide a good fit to the data, and are in agreement with a radially extended warm corona having a size of a few tens of gravitational radii.

**Key words.** Galaxies: active - Galaxies: quasars: individual: HE1029-1401 - X-rays: galaxies

## 1. Introduction

Active Galactic Nuclei (AGN) are highly energetic astrophysical sources powered by the accretion of matter onto a supermassive black hole (SMBH). AGN emit radiation across the whole electromagnetic spectrum. The accretion disk is the primary source of optical/UV emission, while X-ray emission is the result of the inverse Compton scattering of disk optical/UV photons by the hot thermal distribution of electrons that constitute an optically thin corona. This physical mechanism explains the observed power-law shape and the high-energy cut-off often observed at 100 – 150 keV (Malizia et al. 2014; Fabian et al. 2015; Tortosa et al. 2018). The reflection of the primary coronal emission by surrounding material can produce a reflection continuum characterized by a Compton hump peaked at 20 – 30 keV (e.g. George & Fabian 1991; Ricci et al. 2018) and fluorescence emission lines from heavy elements, in particular neutral/ionized Fe K emission is ubiquitous in AGN spectra.

The soft X-ray excess is frequently observed in the spectra of unobscured AGN (e.g. Walter & Fink 1993; Page et al. 2004; Bianchi et al. 2009; Gliozzi & Williams 2020). Currently, the most debated scenarios for the origin of the soft excess are the two-corona model and the model involving relativistic ionized reflection (e.g. Crummy et al. 2006; Walton et al. 2013; García

et al. 2016). The first involves a warm optically thick corona and a hot optically thin corona, with the soft excess originating from the Comptonization of optical/UV photons from a warm electron corona with values of optical depth ( $\tau^w$ ) and electron temperature ( $kT_e^w$ ) being, respectively, 10 – 20 and  $\approx 1$  keV (e.g. Magdziarz et al. 1998; Mehdipour et al. 2011; Jin et al. 2012; Mehdipour et al. 2015; Petrucci et al. 2018; Porquet et al. 2018, and references therein). The second model explains the soft excess as the reprocessing of the primary continuum off an ionised disk (Ross & Fabian 1993), with the soft excess profile being due to the overlapping of blurred soft X-ray emission lines.

In this paper, we investigate the properties of the hot corona and the physical origin of the soft excess in the radio-quiet quasar HE 1029-1401. HE 1029-1401 ( $z = 0.086$  Wisotzki et al. 1991) is a bright quasar hosting a SMBH of mass  $\log(M_{\text{BH}}/M_{\odot}) = 8.7 \pm 0.3$  (Husemann et al. 2010). HE 1029-1401 was discovered in the 1980s by the Edinburgh-Cape Blue Object (EC) Survey with the UK-Schmidt telescope at the Anglo Australian Observatory (AAO) but was confirmed as a quasar only thanks to the Hamburg/ESO Survey which investigated the southern extragalactic sky in 1990 (Wisotzki et al. 1991). With an apparent magnitude  $V = 13.6$ , at the time of discovery it was the brightest quasar ever found in the optical. The source has a bolometric luminosity  $\log(L_{\text{bol}}/[\text{erg s}^{-1}]) = 46.0 \pm 0.2$  corre-

Table 1: Obs. ID, start date and exposure time for HE 1029-1401 *XMM-Newton* and *NuSTAR* observations.

Satellite	Obs. ID	Start time (UTC)	Net exp.(s)
<i>XMM-Newton</i>	0890410101	2022-05-23	$7.14 \times 10^4$
<i>NuSTAR</i>	60701046002	2022-05-23	$2.24 \times 10^5$

sponding to an Eddington rate of  $\log(L_{\text{bol}}/L_{\text{Edd}}) = -0.9 \pm 0.2$  (Husemann et al. 2010). The first detection of the X-ray emission of this AGN occurred thanks to the Japanese satellite *Ginga*. The X-ray spectrum studied by Iwasawa et al. (1993), showed a flat power law and an excess of emission in the soft band. More recently, HE 1029-1401 has been included in the sample studied by Petrucci et al. (2018); the authors used a large sample of radio-quiet AGN, observed by *XMM-Newton*, to test the possible origin of the soft excess from a warm corona. The model provides a good fit to the *XMM-Newton* data, however the lack of high-energy coverage does not allow for tight constraints on the reflection component. This paper reports on the analysis of a simultaneous *XMM-Newton* and *NuSTAR* observation performed in May 2022.

The paper is structured as follows: Sect. 2 describes the observations and data reduction, Sect. 3 presents the analysis of the *XMM-Newton* and *NuSTAR* spectra, first focused on the hard X-ray band and then extended to the broad X-ray band. In Sect. 4 we discuss the results and we present our conclusions.

## 2. Observations and data reduction

*XMM-Newton* observed the source with the optical monitor (OM; Mason et al. 2001) and the EPIC cameras (Strüder et al. 2001; Turner et al. 2001). We processed the data using the *XMM-Newton* Science Analysis System (SAS v20). The OM photometric filters U, UVW1, UVM2, and UVW2 were used, in the image mode, for a total exposure time of 21 ks each. We processed the OM data with the SAS pipeline omichain<sup>1</sup>, and converted to OGIP format with the SAS task om2pha. The EPIC-pn and MOS cameras operated in the Small Window mode meaning a live time of 71%. We use only pn data for the spectral analysis, because of the higher effective area compared with MOS. Moreover, MOS data suffer from low-energy noise, leading to significant residuals below 1-2 keV. However, we verified that the spectral parameters in the 2–10 keV band are consistent among MOS and pn, even though with larger uncertainties in MOS. No significant pile-up is found using the SAS task epatplot. We determined source extraction radii and screening for high-background intervals via an iterative process that maximizes the signal-to-noise ratio, following Piconcelli et al. (2004). We extracted the background from circular regions with a radius of 50 arcsec. Source radii were allowed to be in the range 20–40 arcsec, and the best radius was found to be 40 arcsec. To generate the effective area, we used the SAS task arfgen with the keyword applyabsfluxcorr=yes, which improves the agreement with the *NuSTAR* spectra. Finally, the pn spectra were grouped to have at least 30 counts in each bin, and not oversampling the spectral resolution by a factor greater than 3.

We reduced the *NuSTAR* data with the standard pipeline (nupipeline) of the *NuSTAR* Data Analysis Software (nustardas,

<sup>1</sup> The standard omichain task applies flat-field corrections, detects sources, computes source positions and their count rates, and applies the proper calibration to convert to instrumental magnitudes. HE 1029-1401 is by far the brightest source in the field of view, and its count rates are extracted from a region of 5.3 arcsec.

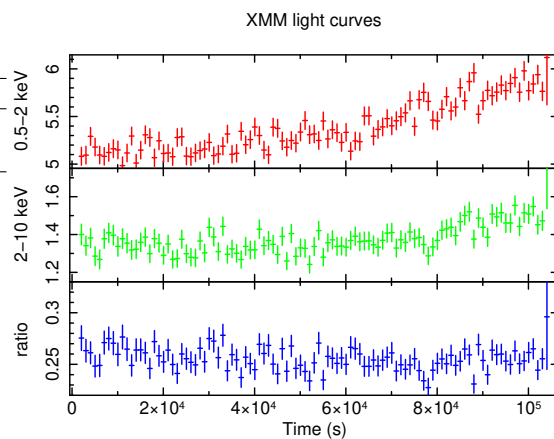


Fig. 1: *XMM* count rate light curves. Top panel: light curve for the energy interval 0.5 – 2 keV. Middle panel: light curve for the energy interval 2 – 10 keV. Bottom panel: ratio between the two energy band.

v1.9.7), using calibration files from *NuSTAR* caldb v20221229. We extracted spectra and light curves with the standard tool nuproducts for the two detectors in focal plane modules A and B (FPMA and FPMB). We extracted the background data from circular regions with a radius of 75 arcsec, while the source radii were calculated to maximize the signal-to-noise like for *XMM-Newton*. The final source radii were 80 arcsec. We regrouped the spectra with the tool ftgrouppha, part of HEASOFT v6.31.1, according to the optimal scheme of Kaastra & Bleeker (2016) with the additional requirement of a minimum signal-to-noise of 3 in each bin. The spectra from FPMA and FPMB were analysed jointly but not co-added. To account for the cross-calibration between the two *NuSTAR* modules, we included a constant term in the spectral fits. We find a difference of 2% between the two modules. The log of the data sets analysed in this paper is listed in Table 1.

The *XMM-Newton* and *NuSTAR* light curves of HE 1029-1401 are plotted in Figure 1 and Figure 2 respectively. The light curves shows an X-ray variability, but no hardness ratio variation is observed. The observation occurred in a low flux period ( $\approx 1 \times 10^{11} \text{ erg s}^{-1} \text{ cm}^{-2}$ ) and for *NuSTAR* the background was particularly high dominating over the source at energies greater than 30 keV. For these reasons, we exclude the *NuSTAR* data above 30 keV for the spectral analysis.

## 3. Spectral analysis

We performed the spectral analysis with the *xspec* v12.13.0 package (Arnaud 1996). Fits were performed on the rebinned pn and *NuSTAR* spectra plus the OM photometric data, using the  $\chi^2$  minimization technique. All errors are quoted at the 90% confidence level ( $\Delta\chi^2 = 2.71$ ) for one interesting parameter. In all of our fits, we included neutral absorption (TBABS model in *xspec*) from Galactic hydrogen with column density  $N_{\text{H}} = 5.74 \times 10^{20} \text{ cm}^{-2}$  (Kalberla et al. 2005). The cosmological parameters  $H_0 = 70 \text{ km s}^{-1} \text{ Mpc}^{-1}$ ,  $\Omega_{\Lambda} = 0.73$  and  $\Omega_m = 0.27$  are adopted.

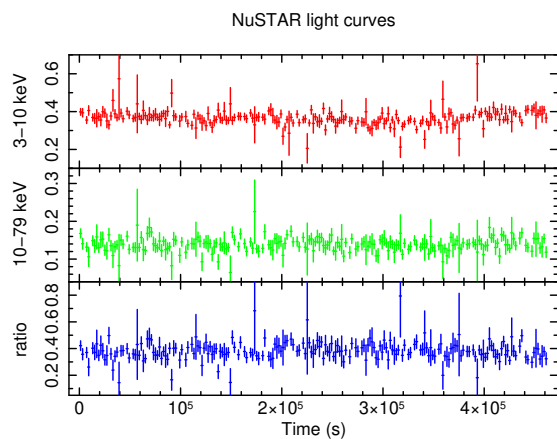


Fig. 2: *NuSTAR*/FPMA background-subtracted count rate light curves. Top panel: light curve for the energy interval 3 – 10 keV. Middle panel: light curve for the energy interval 10 – 79 keV. Bottom panel: ratio between the two energy band.

### 3.1. The reflection component

We started by investigating the Fe  $K\alpha$  line at 6.4 keV. Initially, we constructed the spectra solely based on a power law model. Figure 3 illustrates the ratio between the observed data and the model derived from this initial fit. It reveals an amplification in the data/model ratio up to 5 keV, along with an emission line at 6.4 keV. To address this, we introduced a single Gaussian line with a fixed energy of 6.4 keV and a fixed sigma of zero; in this first part, we analysed only the *XMM-Newton*/pn spectrum in the 3-10 keV band, given the much better energy resolution compared with *NuSTAR*. The resulting  $\chi^2/\text{d.o.f.}$  was 128/104. Subsequently, leaving the intrinsic width free to vary we found a reduced  $\chi^2/\text{d.o.f.}$  of 121/103. Despite the modest enhancement observed, we proceeded with further test. We modeled the data using two emission lines, both located at 6.4 keV, one narrow ( $\sigma = 0$ ) and one broadened due to relativistic effects ( $\sigma$  free to vary). In this case, we found a significant improvement, with  $\chi^2/\text{d.o.f.} = 114/102$  ( $\Delta\chi^2/\Delta\text{d.o.f.} = -24/-2$ ). The broad emission line has  $\sigma = 0.38^{+0.26}_{-0.16}$  keV.

We concluded that the data are consistent with the presence of both a narrow and a broad emission line.

As a next step, we fitted jointly the *XMM-Newton*/pn and *NuSTAR* data in the 3–30 keV band with a self-consistent reflection model. Since we found evidence of both a narrow and a broad component of the Fe  $K\alpha$  emission line, we included two different reflection components. Our model consists of a power law with an exponential cut-off ( $E_{\text{cutoff}}$ ), a non-relativistic reflection component (XILLVER García & Kallman 2010; García et al. 2013) and a relativistic one (RELXILL García et al. 2014; Dauser et al. 2016).<sup>2</sup> We fixed the source inclination angle at  $30^\circ$ , the outer radius of the accretion disk to  $400 R_g$  and the spin of the black hole to 0.998. This leaves us with the freedom to vary the internal radius of the accretion disk, as the internal disk radius and spin parameter are degenerate. The value of the photon index in RELXILL - as in XILLVER - was linked to that of the continuum. The ionization parameter in XILLVER was fixed at  $\log \xi = 0$ , while in RELXILL is left free to vary. All the other components were free to vary. With this model, we obtained an acceptable fit with  $\chi^2/\text{d.o.f.} = 338/303$  and the following best-fit parameters:  $R_{\text{int}}$

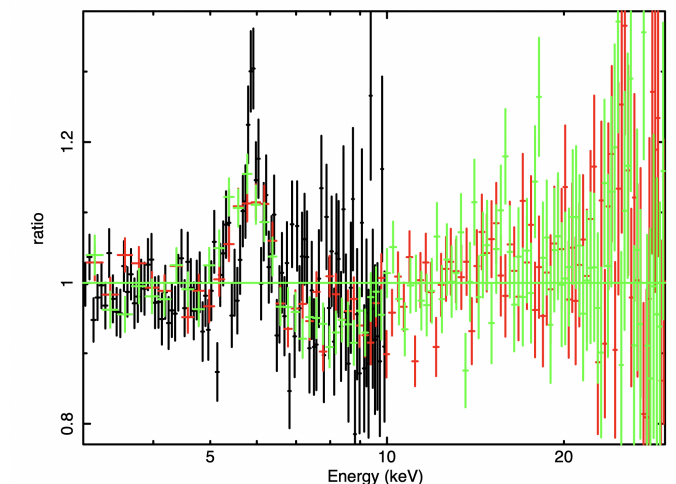


Fig. 3: Data/model ratio for the *XMM-Newton* and *NuSTAR* spectrum in the 3-30 keV band using the model:  $\text{CONST} \times \text{TBABS} \times \text{CUTOFFPL}$ .

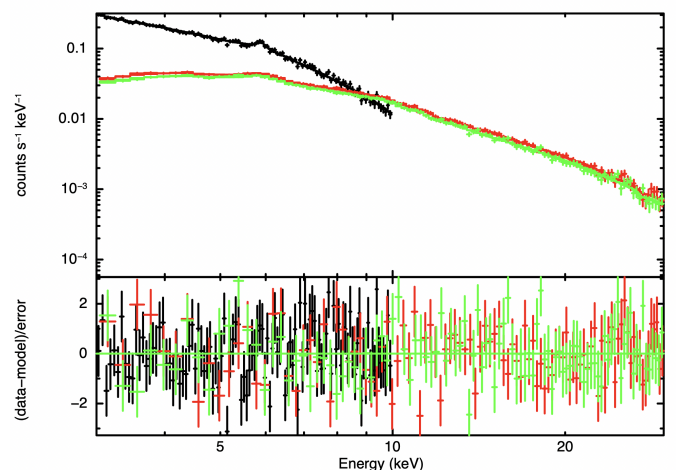


Fig. 4: Upper panel: Spectroscopic data and best fit model between 3 and 30 keV. Lower panel: residuals of the model. Model used during the fit:  $\text{CONST} \times \text{TBABS} \times (\text{CUTOFFPL} + \text{RELXILL} + \text{XILLVER})$ . *XMM-Newton* data are in black, the *NuSTAR* FMPA data in red and the *NuSTAR* FMPB data in green.

$= 30^{+8}_{-7} R_g$ ,  $A_{\text{Fe}} = 1.7^{+0.4}_{-0.3}$ ,  $\Gamma^h = 1.79 \pm 0.02$ ,  $E_{\text{cutoff}} = 84^{+20}_{-12}$  keV and  $\log(\xi/\text{erg cm s}^{-1}) = 1.0^{+0.6}_{-0.5}$ . In Fig. 4 we plot the spectra and the residuals of the model.

### 3.2. Soft excess and relativistic reflection

After the analysis of the reflection component, we fitted the whole *XMM-Newton* and *NuSTAR* data in the 0.35-30 keV band. In our case, thanks to the high *NuSTAR* sensitivity in the hard X-rays, we can better constrain the reflection component and the primary continuum at high energies.

The soft excess is clearly visible in Fig. 5, which represents the data in the entire available energy range and the best fit model discussed in the previous section. We first tested a phenomenological model for the soft excess, namely a disk blackbody component (DISKBB in XSPEC). We left free to vary the inner temper-

<sup>2</sup>  $\text{TBABS} \times (\text{CUTOFFPL} + \text{RELXILL} + \text{XILLVER})$

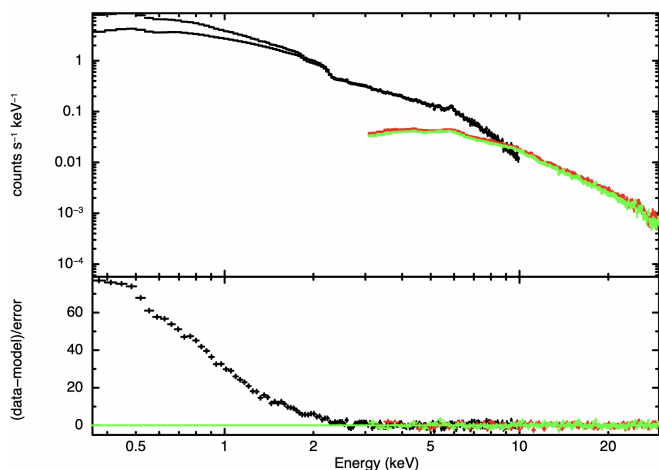


Fig. 5: Upper panel: Spectroscopic data between 0.35 and 30 keV and best fit model. Lower panel: residuals of the model. Model used during the fit:  $\text{TBABS} \times (\text{CUTOFFPL} + \text{RELXILL} + \text{XILLVER})$ . *XMM-Newton* data are in black, the *NuSTAR FMPA* data in red and the *NuSTAR FMPB* data in green.

ature of the disk and the normalization of `DISKBB`. For the temperature, a best fit value of  $172 \pm 7$  eV was found.

Then, we tested whether a model including only reflection components is able to explain the soft excess.

We tested two different flavors of `XILLVER` and `RELXILL`. In the first case, we used the model  $\text{CONST} \times \text{TBABS} \times (\text{CUTOFFPL} + \text{RELXILL} + \text{XILLVER})$  (model A). We employed `RELXILL` to characterize both the continuum and the ionized reflection originating from the inner disc, which generate a soft excess in this model. Additionally, `XILLVER` was utilized for the constant reflection component. In `RELXILL`, the free parameters were the ionization and the normalization, while the iron abundance is tied to the value of `XILLVER`. The outer disk radius was fixed at  $400 R_g$ , while the inner disk radius was left free to vary during the fit. The value of the photon index and of the cut-off energy in `RELXILL` - as in `XILLVER` - were linked to those of the continuum. With this model, we found an unacceptable fit with  $\chi^2/\text{d.o.f.} = 790/369$  and strong residuals below 1 keV. We also tried to include a warm absorber (modeled with a `CLOUDY` table, [Ferland et al. 2013](#) computed assuming a standard type 1 AGN illuminating spectrum) to model the residuals, but no significant improvement was found (even in this case we found a reduced  $\chi^2 > 2$ ).

For the second model (model B) we used `RELXILLD` and `XILLVERD`, that includes the density of the reflecting material as a free parameter ([García et al. 2016](#)).<sup>3</sup> Free-free absorption is directly proportional to density squared, so an uptick in density results in additional thermal emissions from the disk. During the fit, we left the disk density free to vary without imposing a link between the two components. The other parameters were set as in model A. Even in this case, we found a poor fit with  $\chi^2/\text{d.o.f.} = 694/367$ . For the residuals of the fit see Fig. 6. With this model we found the following best fit parameters for the two densities:  $\log N[\text{cm}^{-3}] = 17.69^{+0.01}_{-0.03}$  and a lower limit at  $\log N[\text{cm}^{-3}]$  of 18.97.

In the `relxilld` framework, the maximum density considered is  $10^{19} \text{cm}^{-3}$ . Therefore, we attempted to fit the data using a model incorporating a high-density component to char-

acterize the reflection (`REFLIONXHD`), which supports densities up to  $10^{22} \text{cm}^{-3}$ . In this model (referred to as model C<sup>4</sup>), we convolved `reflionxhd` with `kdblur` to account for relativistic effects. Instead of `xillver`, we utilized `reflionxhc` to describe the reflection, which calculates the reflected spectrum for optically-thick material of constant density. Additionally, we introduced a warm absorber (also using a `CLOUDY` table) in an attempt to better model the soft emission. However, we still obtained a poor fit ( $\chi^2/\text{d.o.f.} = 683/366$ ) with a density of  $(7.64 \pm 1.22) \times 10^{17} \text{cm}^{-3}$ .

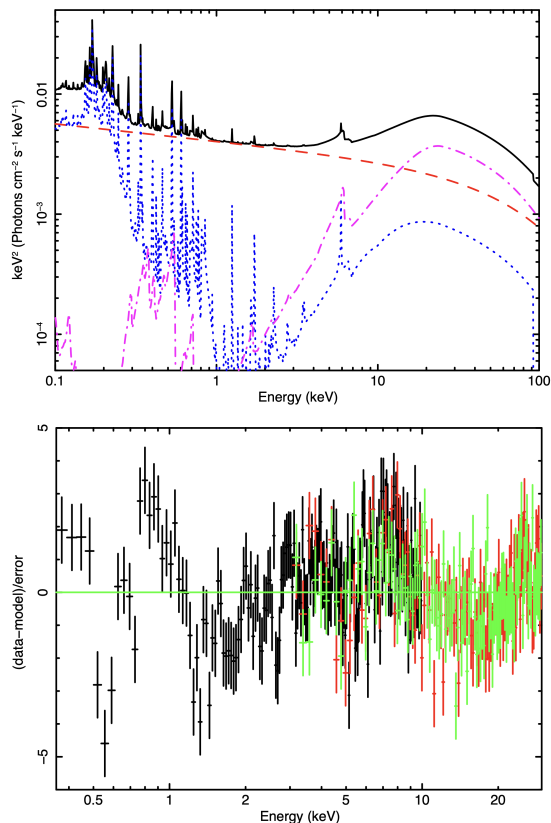


Fig. 6: Upper panel: Model B ( $\text{CUTOFFPL} + \text{RELXILLD} + \text{XILLVERD}$ ) of the X-ray spectrum of HE 1029-1401. The solid thicker black line is the best-fit model while the dashed lines are the different spectral components: in red the emission of the hot corona, the non-relativistic reflection component in blue and the relativistic reflection in pink.

Lower panel: residuals of the model. *XMM-Newton* data are in black, the *NuSTAR FMPA* data in red and the *NuSTAR FMPB* data in green. Model used during the fit: model B.

### 3.3. Testing the two corona model

In this section, we studied HE 1029-1401 using the two-corona model. In this model (model D), the soft X-ray spectrum is reproduced only by a thermally Comptonized continuum, modeled using `NTHCOMP` in *xspec*. The hard X-ray band is also modeled with `NTHCOMP`, which parameterizes the high-energy roll-over using the electron temperature.<sup>5</sup> In model D for the characterization of the reflection component, we replaced `RELXILL` and `XILLVER` with `RELXILLCP` and `XILLVERCP`, fitting for the electron temperature in-

<sup>4</sup> model C:  $\text{CONST} \times \text{TBABS} \times \text{CLOUDY} (\text{CUTOFFPL} + \text{REFLIONXHC} + \text{KDBLUR} \times \text{REFLIONXHD})$

<sup>5</sup> model D:  $\text{CONST} \times \text{TBABS} \times (\text{NTHCOMP} + \text{NTHCOMP} + \text{RELXILLCP} + \text{XILLVERCP})$

<sup>3</sup> model B:  $\text{CONST} \times \text{TBABS} \times (\text{CUTOFFPL} + \text{RELXILLD} + \text{XILLVERD})$

stead of the exponential cut-off. We fixed the inclination angle at  $30^\circ$ , the outer radius of the accretion disk at  $400 R_g$ , and the spin of the black hole at 0.998. During the fit, we assumed that seed photons arise from a multicolor accretion disk, and all other parameters were left free to vary.

Using this approach, we obtained an acceptable fit with a  $\chi^2/\text{d.o.f.} = 429/365$ . In an attempt to represent the residuals in the soft band, we tried to include a warm absorber (modelled using the spectral synthesis code `CLOUDY`, as in the previous section) but no significant improvement was observed. We then extended our spectral investigation to the optical-UV domain by including the OM data in the fit (model E). [Petrucci et al. \(2018\)](#) applied a model to the archival *XMM-Newton*/OM and pn data of the source, incorporating two `NTHCOMP` components ([Zdziarski et al. 1996](#); [Życki et al. 1999](#)) to represent the Comptonization continuum originating from the two coronae. Additionally, they included a single non-relativistic reflection component and a component to account for the contribution of the broad-line region (BLR) in the optical/UV band.<sup>6</sup> In the same way of [Petrucci et al. \(2018\)](#), we considered the potential influence of the broad-line region on the spectra including a model for the small blue bump, formed by the Balmer continuum together with Fe II emission. Our approach is based on an additive table with freely adjustable normalization (`SMALLBB`)<sup>7</sup>. A comprehensive description of this table for NGC 5548 is provided by [Mehdipour et al. \(2015\)](#). We, as well as [Petrucci et al. \(2018\)](#), also included the effect of Galactic extinction (using the `REDDEN` function in `xspec`), with the reddening fixed during the fit at  $E(B - V) = 0.0954$  ([Güver & Özel 2009](#)).<sup>8</sup> The fit resulted in a chi-squared value of  $\chi^2/\text{d.o.f.} = 437/368$ . Specifically, the fit showed a not very much ionized accretion disk ( $\log(\xi/\text{erg cm s}^{-1}) = 1.30^{+0.24}_{-0.12}$ ), an internal radius of the accretion disk equal to  $32^{+23}_{-10} R_g$ , and a photon index and an electron temperature  $\Gamma^h = 1.86 \pm 0.02$  and  $kT_e^h = 17^{+4}_{-2}$  keV for the hot corona and  $\Gamma^w = 2.75 \pm 0.05$  and  $kT_e^w = 0.39^{+0.04}_{-0.03}$  keV for the warm corona.

The optical depth of the corona is not one of the fit parameters but can be obtained, starting from the index  $\Gamma$  and the temperature of the electrons, using the relation from [Pozdnyakov et al. \(1977\)](#):

$$\tau_e = \sqrt{2.25 + \frac{3}{\theta_e(\Gamma + 0.5)^2 - 2.25}} - 1.5, \quad (1)$$

where  $\theta_e$  is the electron temperature normalized to the electron rest energy. For the hot and warm corona we find, respectively:  $\tau^h = 5.4 \pm 0.9$ , and  $\tau^w = 23 \pm 3$ .

The fitting parameters are reported in Table 2. Fig. 8 shows the spectra and residuals of the model E, while in Fig. 9 the best-fit model is represented. According to this model, the broad-band spectrum of HE 1029-1401 is well described by two Comptonization processes. Specifically, the hard X-ray emission is primarily due to Comptonization in the hot corona, while the optical/UV to soft X-ray emission is dominated by Comptonization

<sup>6</sup> `TBABS`  $\times$  `REDDEN`  $\times$  `MTABLE`{`CLOUDYTABLE`}  $\times$  (`NTHCOMP` + `NTHCOMP` + `ATABLE`{`SMALLBB`} + `ATABLE`{`GALAXY`} + `XILLVER`)

<sup>7</sup> The contribution by the host galaxy is not strong, being a factor of 10 below the nuclear flux both in the optical band ([Husemann et al. 2010](#)) and in the UV band (estimated with `GALFIT`; K. K. Gupta, private communication). Given the coarse resolution of the OM photometric filters, and the fact that most of the filters used here are in the UV band, we opt to include only the BLR emission component, which dominates in the UV band over the galaxy ([Mehdipour et al. 2015](#)).

<sup>8</sup> model E: `CONST` $\times$ `TBABS` $\times$ `REDDEN` $\times$ (`NTHCOMP`+`NTHCOMP`+`SMALLBB`+`RELXILLCP`+`XILLVERCP`)

in a warm corona. The potential degeneracy of the hot corona temperature with the reflection fraction has been investigated, yet no indications of degeneracy were observed (see Fig. 7). The absorption-corrected model luminosity in the 0.001–1000 keV band is  $6 \times 10^{45} \text{ erg s}^{-1}$ , corresponding to an Eddington ratio of  $\sim 0.1$ .

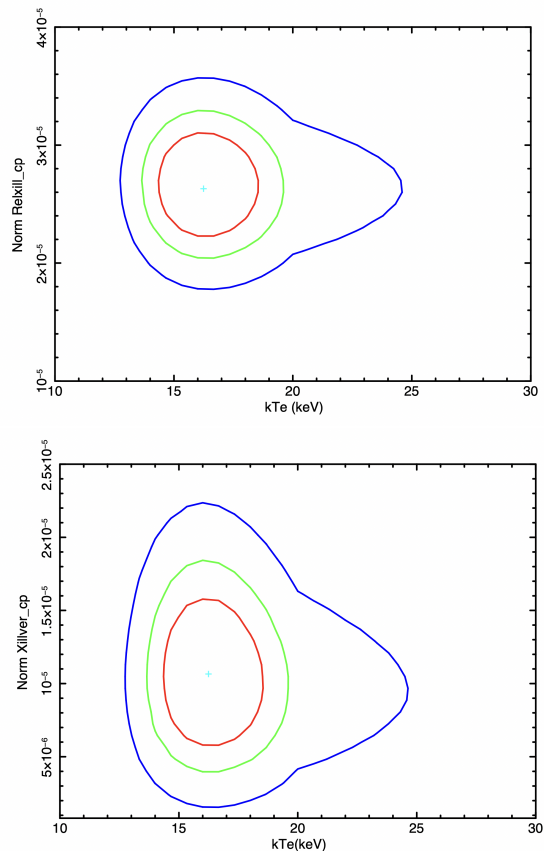


Fig. 7: Upper panel: Contour plot of `RELXILLCP` normalization versus electron temperature in the hot corona. Lower panel: Contour plot of `XILLVERCP` normalization versus electron temperature in the hot corona. The solid blue, green, and red curves represent the 68%, 90%, and 99% confidence levels, respectively. Both plots are generated using model E.

As a further step in model F, we replaced the warm `NTHCOMP` component with a table model computed by [Petrucci et al. \(2020\)](#), who performed numerical simulations of the spectra of warm coronae using the radiative transfer code `TITAN` coupled with the Monte-Carlo code `NOAR` ([Dumont et al. 2003](#)). This model, in its current implementation, assumes a black body seed photon spectrum, instead of a disk black body assumed in `NTHCOMP`.<sup>9</sup> The free parameters of the `TITAN` table are the black body temperature of the seed photons, the heating power  $q_h$  in the warm corona, the optical depth  $\tau^w$ , and the normalization. During this fit, we left all the parameters of the `TITAN` table free to vary. The temperature of the seed photons in the `NTHCOMP` model that describes the hot corona was linked to that of the `TITAN` table. With this model, we found a chi-squared value of  $\chi^2/\text{d.o.f.} = 443/368$  and the following best fit parameters for the warm corona. For the logarithm of the heating power  $\log q_h$  ( $\text{erg s}^{-1} \text{ cm}^3$ ) we found  $-22.862^{+0.002}_{-0.004}$ , for the logarithm of  $T_{bb}$

<sup>9</sup> model F: `CONST` $\times$ `TBABS` $\times$ `REDDEN` $\times$ (`NTHCOMP`+`TITAN`+`SMALLBB`+`RELXILLCP`+`XILLVERCP`)

Table 2: Best-fitting parameters of model E described in Sect. 3.3.

$\log \xi_i$	$\text{erg s}^{-1} \text{ cm}$	$1.30^{+0.24}_{-0.12}$
$A_{\text{Fe}}$		$2.2^{+0.7}_{-0.6}$
$N_{\text{xill}}(10^{-5})$	$\text{ph keV}^{-1} \text{ cm}^{-2} \text{ s}^{-1}$	$1.0 \pm 0.5$
$R_{\text{int}}$	$R_g$	$32^{+23}_{-10}$
$N_{\text{rel}}(10^{-5})$	$\text{ph keV}^{-1} \text{ cm}^{-2} \text{ s}^{-1}$	$2.7 \pm 0.6$
$N_{\text{small-bb}}(10^{-2})$	$\text{ph keV}^{-1} \text{ cm}^{-2} \text{ s}^{-1}$	$1.8 \pm 0.9$
$\Gamma^{\text{w}}$		$2.75 \pm 0.05$
$kT_e^{\text{w}}$	$\text{keV}$	$0.39^{+0.04}_{-0.03}$
$kT_{\text{bb}}^{\text{w}}$	$\text{eV}$	$2.9 \pm 0.5$
$N_{\text{NthComp}}^{\text{w}}(10^{-3})$	$\text{ph keV}^{-1} \text{ cm}^{-2} \text{ s}^{-1}$	$1.39^{+0.13}_{-0.11}$
$\Gamma^{\text{h}}$		$1.86 \pm 0.02$
$kT_e^{\text{h}}$	$\text{keV}$	$17^{+4}_{-2}$
$N_{\text{NthComp}}^{\text{h}}(10^{-3})$	$\text{ph keV}^{-1} \text{ cm}^{-2} \text{ s}^{-1}$	$3.81^{+0.11}_{-0.12}$
$F_{0.5-2}(10^{-12})$	$\text{ergs s}^{-1} \text{ cm}^{-2}$	$8.04^{+0.03}_{-0.02}$
$F_{2-10}(10^{-11})$	$\text{ergs s}^{-1} \text{ cm}^{-2}$	$1.07 \pm 0.01$
$L_{0.5-2}(10^{43})$	$\text{ergs s}^{-1}$	$1.49 \pm 0.01$
$L_{2-10}(10^{44})$	$\text{ergs s}^{-1}$	$1.94 \pm 0.01$

(in unit of K)  $4.38 \pm 0.05$ , for the optical depth  $\tau^{\text{w}} = 18.4^{+0.4}_{-0.6}$  and the normalization was  $1.53^{+0.13}_{-0.16} \times 10^{-4}$ . Given the source distance and luminosity, from the model we can also estimate the radial size of the warm corona. The normalization of the table is indeed directly related to this quantity, with some simple counts (see [Petrucci et al. 2020](#)) we obtained  $\sim 20 R_g$ .

Finally in model G, we tested the model `REXCOR` by [Xiang et al. \(2022\)](#) (see also [Ballantyne & Xiang 2020](#); [Ballantyne et al. 2024](#)), which incorporates both warm Comptonization and ionized reflection from a warm corona illuminated by a lamp-post hot corona. In this model, the accretion energy is distributed between the disk, the warm corona and the hot corona. The relative strength of warm Comptonization and of ionized reflection is driven by the heating fraction of the warm corona and of the hot corona, respectively. The model does not include optical/UV

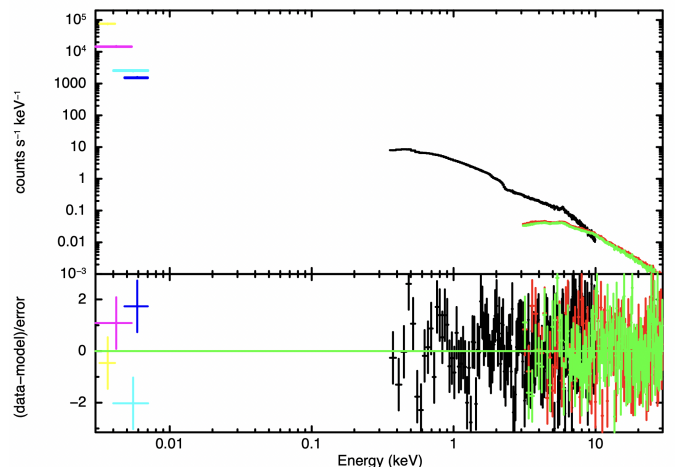


Fig. 8: Upper panel: HE 1029-1401 data and best fit model. Lower panel: residuals of the model. Model used during the fit: model E. *XMM-Newton* data are in black, the *NuSTAR FMPA* data in red and the *NuSTAR FMPB* data in green.

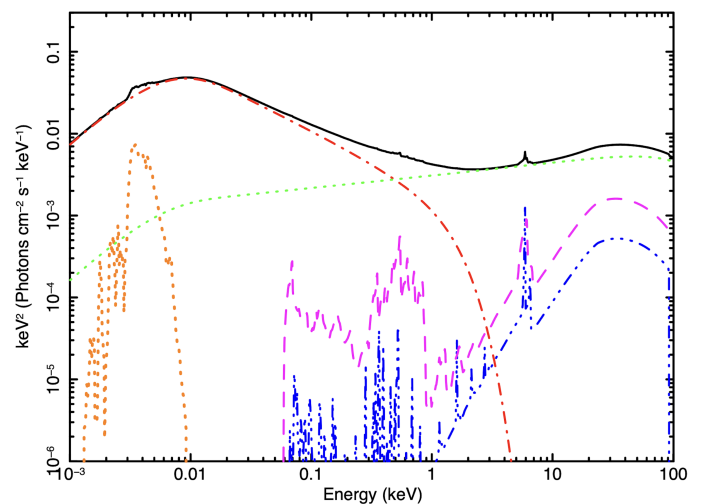


Fig. 9: Best-fit model of the UV/X-ray spectrum of HE 1029-1401. The solid thicker black line is the best-fit model while the dashed lines are the different spectral components: in green the emission of the hot corona, in red the emission of the warm corona, the non-relativistic reflection component in blue, the relativistic reflection in pink and in orange the contribution of the small blue bump.

emission, thus for simplicity we fitted only the X-ray spectra. Since `REXCOR` includes blurred ionized reflection, we replaced both the warm Comptonization component and the `RELXILL` reflection component with `REXCOR`.<sup>10</sup> We kept the `XILLVERCP` component to reproduce distant reflection. In `REXCOR` we assumed a lamp-post height of  $20 R_g$ , a black hole spin of 0.99, and an Eddington ratio of 0.1 consistent with the results reported by [Ballantyne et al. \(2024\)](#). We initially found a poor fit in the soft band with strong residuals near 0.5 keV. To account for these, we included two narrow Gaussian absorption lines, which are found to be at 0.62 keV and 0.74 keV. Gaussian lines of this type, here briefly described, are often needed in this kind of fit, see for example [Ballantyne et al. \(2024\)](#). We obtained an acceptable fit

<sup>10</sup> model G: `TBFEOXCONST(XILLVERCP+REXCOR+NTHCOMP)`

with  $\chi^2/\text{d.o.f.} = 436/364$  and the following best-fit parameters for `reXCOR`: hot corona heating fraction  $f_X = 0.030^{+0.015}_{-0.003}$ , warm corona heating fraction  $0.40^{+0.05}_{-0.03}$  and optical depth  $\tau < 11$  (the lower limit of the model is 10).

#### 4. Discussion and conclusions

The origin of the soft excess in the X-ray spectra of AGN is still debated. Here we have presented the analysis of XMM-Newton and NuSTAR simultaneous observation of the nearby ( $z=0.086$ ) AGN HE 1029-1401 with the aim of revealing the nature of the soft-excess in this source. Our findings can be summarized as following:

- The spectrum of the source shows the presence of a narrow Fe  $K\alpha$  line and a broad ( $\sigma = 0.38^{+0.26}_{-0.16}$  keV) Fe  $K\alpha$  line, at 6.4 keV.
- To account for emissions resulting from reflection, it was essential to incorporate both a relativistic and a non-relativistic component into the best fit model.
- The study confirms the presence of a significant soft X-ray excess below 2 keV. No warm absorber has been detected.
- We find that the two corona model describes the source better than the reflection model. With a phenomenological model we measure for the hot corona a relatively low temperature  $kT_e^h = 17^{+4}_{-2}$  keV, and an optical depth of  $\tau^h = 5.40 \pm 0.85$  (assuming a spherical geometry); for the warm corona, we obtain parameters consistent with lower luminosity Seyferts:  $\Gamma^w = 2.75 \pm 0.05$ ,  $kT_e^w = 0.39^{+0.06}_{-0.04}$  keV,  $\tau^w = 23 \pm 3$ .
- We have also tested two more physical models for the warm corona, namely the TITAN-NOAR table model by [Petrucci et al. \(2020\)](#), and the `reXCOR` model by [Xiang et al. \(2022\)](#). Despite the different physical assumptions (for a more detailed comparison, see [Petrucci et al. 2020](#)), both models provide a good fit to the data. The results are consistent with the presence of a warm corona with an optical depth of the order of 10–20 and with a radial extension of a few tens of gravitational radii.

This is the first *NuSTAR* observation of the source. However, previous X-ray observations of this source were conducted using the *XMM-Newton* telescope and were analyzed in a previous paper by [Petrucci et al. \(2018\)](#). The results for the warm corona reported in the current study are comparable with those reported in the previous paper indicating consistency between the two studies. Specifically, for the hot corona we found slightly different parameters due to a different assumption in the temperature of the hot electrons. The results obtained in Model G can be compared with the analysis of another observation of the source using the same model as reported in [Ballantyne et al. \(2024\)](#). Our work yields a hot corona heating fraction that is compatible with that of [Ballantyne et al. \(2024\)](#), alongside a lower value for the warm corona heating fraction and a slightly larger photon index. We also computed the ratio of the 0.3–10 keV `reXCOR` and primary continuum fluxes; we obtain a value of 0.36, compatible with [Ballantyne et al. \(2024\)](#). Our results are overall consistent with the trends between the `reXCOR` parameters and the Eddington ratio discussed by [Ballantyne et al. \(2024\)](#), see their Fig. 1–4. We can compare the results obtained with an other quasar for which the two coronae model was tested: RBS 1055 ([Marinucci et al. 2022](#)). In our study, we have observed that the coronae of RBS 1055 are hotter compared to those found for HE 1029-1401 in this study. This could be due to a number of factors such as differences in the physical properties of the black

hole or the surrounding environment, or variations in the accretion rate and efficiency. Indeed the Eddington ratio of HE 1029-1401 is a factor two larger than the Eddington ratio of RBS 1055 ( $L_{\text{bol}}/L_{\text{Edd}} \simeq 0.05$ ).

In a wider scenario, the values obtained from this study align with those known for radio-quiet AGNs described by the two coronae model (see [Petrucci et al. 2018](#)): a warm corona, with an optical depth  $\tau \simeq 10 - 40$  and an electron temperature  $kT \simeq 0.1 - 1$  keV and a hot corona, optically thin ( $\tau \simeq 1$ ) and hot ( $kT > 20$  keV).

In conclusion, the two-corona model provides a good fit of the data, indicating that warm Comptonization is a likely explanation for the soft excess. The broad-band UV/X-ray properties of this luminous quasar are overall consistent with those of local Seyferts, hinting at a similar structure of the accretion flow. This is broadly consistent with the results of [Mitchell et al. 2023](#), who analyse the spectral energy distribution of a large sample of quasars at  $z \leq 2.5$  and find that the spectral shape of the optical-UV continuum remains nearly constant across decades of black hole mass for a given luminosity. [Mitchell et al. 2023](#) point out that standard accretion disc models cannot reproduce this behavior, which can instead be explained if the disc is completely covered by a warm Comptonising corona, as long as the UV spectral shape correlates with the accretion rate (which is indeed observed, see [Petrucci et al. 2018](#)). In our case, we find a relatively steep photon index of the warm corona, in agreement with the Eddington ratio measured for HE1029-1401.

The existence of the warm corona could yield significant implications, such as directly influencing our comprehension of the vertical equilibrium of the accretion disk. Moreover, models E, F, and G provide a good description of the X-ray spectrum, but their distinct assumptions highlight the necessity for further investigations to enhance our comprehension of warm coronal properties. Future observations of luminous quasars will enable further studies of the soft excess in different accretion regimes.

#### Data Availability

The data analysed in this paper are publicly available via the *XMM-Newton* and *NuSTAR* archives. See Table 1 for the Obs. ID and the details of the observations.

*Acknowledgements.* We thank the referee for useful comments that improved the manuscript. This research was supported by the International Space Science Institute (ISSI) in Bern, through ISSI International Team project #514 (Warm Coronae in AGN: Observational Evidence and Physical Understanding). The research leading to these results has received funding from the European Union's Horizon 2020 Programme under the AHEAD2020 project (grant agreement n. 871158). This publication was produced while B.V. attending the PhD program in in Space Science and Technology at the University of Trento, Cycle XXXVIII, with the support of a scholarship financed by the Ministerial Decree no. 351 of 9th April 2022, based on the NRRP - funded by the European Union - NextGenerationEU - Mission 4 "Education and Research", Component 1 "Enhancement of the offer of educational services: from nurseries to universities" - Investment 4.1 "Extension of the number of research doctorates and innovative doctorates for public administration and cultural heritage". POP acknowledges financial support from the french space agency (CNES) and the High Energy National Programme (PNHE) from CNRS.

#### References

- Arnaud, K. A. 1996, in *Astronomical Society of the Pacific Conference Series*, Vol. 101, *Astronomical Data Analysis Software and Systems V*, ed. G. H. Jacoby & J. Barnes, 17
- Ballantyne, D. R., Sudhakar, V., Fairfax, D., et al. 2024, *MNRAS*[arXiv:2404.03040]

- Ballantyne, D. R. & Xiang, X. 2020, MNRAS, 496, 4255
- Bianchi, S., Guainazzi, M., Matt, G., Fonseca Bonilla, N., & Ponti, G. 2009, A&A, 495, 421
- Crummy, J., Fabian, A. C., Gallo, L., & Ross, R. R. 2006, MNRAS, 365, 1067
- Dauser, T., García, J., Walton, D. J., et al. 2016, A&A, 590, A76
- Dumont, A. M., Collin, S., Paletou, F., et al. 2003, A&A, 407, 13
- Fabian, A. C., Lohfink, A., Kara, E., et al. 2015, MNRAS, 451, 4375
- Ferland, G. J., Porter, R. L., van Hoof, P. A. M., et al. 2013, Rev. Mexicana Astron. Astrofis., 49, 137
- García, J., Dauser, T., Lohfink, A., et al. 2014, ApJ, 782, 76
- García, J., Dauser, T., Reynolds, C. S., et al. 2013, ApJ, 768, 146
- García, J. & Kallman, T. R. 2010, ApJ, 718, 695
- García, J. A., Fabian, A. C., Kallman, T. R., et al. 2016, MNRAS, 462, 751
- George, I. M. & Fabian, A. C. 1991, MNRAS, 249, 352
- Gliozzi, M. & Williams, J. K. 2020, MNRAS, 491, 532
- Güver, T. & Özel, F. 2009, MNRAS, 400, 2050
- Husemann, B., Sánchez, S. F., Wisotzki, L., et al. 2010, A&A, 519, A115
- Iwasawa, K., Kunieda, H., Awaki, H., & Koyama, K. 1993, PASJ, 45, L7
- Jin, C., Ward, M., Done, C., & Gelbord, J. 2012, MNRAS, 420, 1825
- Kaastra, J. S. & Bleeker, J. A. M. 2016, A&A, 587, A151
- Kalberla, P. M. W., Burton, W. B., Hartmann, D., et al. 2005, A&A, 440, 775
- Magdziarz, P., Blaas, O. M., Zdziarski, A. A., Johnson, W. N., & Smith, D. A. 1998, MNRAS, 301, 179
- Malizia, A., Molina, M., Bassani, L., et al. 2014, ApJ, 782, L25
- Marinucci, A., Vietri, G., Piconcelli, E., et al. 2022, A&A, 666, A169
- Mason, K. O., Breeveld, A., Much, R., et al. 2001, A&A, 365, L36
- Mehdipour, M., Branduardi-Raymont, G., Kaastra, J. S., et al. 2011, A&A, 534, A39
- Mehdipour, M., Kaastra, J. S., Kriss, G. A., et al. 2015, A&A, 575, A22
- Mitchell, J. A. J., Done, C., Ward, M. J., et al. 2023, MNRAS, 524, 1796
- Page, K. L., Schartel, N., Turner, M. J. L., & O'Brien, P. T. 2004, MNRAS, 352, 523
- Petrucchi, P. O., Gronkiewicz, D., Rozanska, A., et al. 2020, A&A, 634, A85
- Petrucchi, P. O., Ursini, F., De Rosa, A., et al. 2018, A&A, 611, A59
- Piconcelli, E., Jimenez-Bailón, E., Guainazzi, M., et al. 2004, MNRAS, 351, 161
- Porquet, D., Reeves, J. N., Matt, G., et al. 2018, A&A, 609, A42
- Pozdnyakov, L. A., Sobol, I. M., & Syunyaev, R. A. 1977, Soviet Ast., 21, 708
- Ricci, C., Ho, L. C., Fabian, A. C., et al. 2018, MNRAS, 480, 1819
- Ross, R. R. & Fabian, A. C. 1993, Monthly Notices of the Royal Astronomical Society, 261, 74
- Strüder, L., Briel, U., Dennerl, K., et al. 2001, A&A, 365, L18
- Tortosa, A., Bianchi, S., Marinucci, A., Matt, G., & Petrucci, P. O. 2018, A&A, 614, A37
- Turner, M. J. L., Abbey, A., Arnaud, M., et al. 2001, A&A, 365, L27
- Walter, R. & Fink, H. H. 1993, A&A, 274, 105
- Walton, D. J., Nardini, E., Fabian, A. C., Gallo, L. C., & Reis, R. C. 2013, MNRAS, 428, 2901
- Wisotzki, L., Wamstecker, W., & Reimers, D. L. 1991, A&A, 247, L17
- Xiang, X., Ballantyne, D. R., Bianchi, S., et al. 2022, MNRAS, 515, 353
- Zdziarski, A. A., Johnson, W. N., & Magdziarz, P. 1996, Monthly Notices of the Royal Astronomical Society, 283, 193
- Życki, P. T., Done, C., & Smith, D. A. 1999, MNRAS, 309, 561